A carbon monoxide sensor in polymer electrolyte fuel cells based on symbolic dynamic filtering

K.S. Bhambare [a], S. Gupta [b], M.M. Mench [a,*], A. Ray [b]

[a] *Fuel Cell Dynamics and Diagnostics Laboratory, Department of Mechanical Engineering, The Pennsylvania State University, University Park, 16802, USA*
[b] *Department of Mechanical Engineering, The Pennsylvania State University, University Park, 16802, USA*

ARTICLE INFO

ABSTRACT

Carbon monoxide (CO) dramatically reduces the performance of a fuel cell stack if not remediated. Remediation generally requires parasitic bleeding of a small fraction (<5%) of air into the fuel stream to promote oxidation of the CO and use of a platinum-ruthenium or other noble metal based catalyst. For enhancement of system efficiency, air bleed should be controlled using real-time feedback of CO level in the feed-stream. In this paper, a recently reported data-driven pattern identification method, called Symbolic Dynamic Filtering (SDF), is applied for on-line sensing of CO content in an impure reformed hydrogen fuel stream. A small fuel cell, fuelled by a diverted stream of reformate, is used as a CO sensor. CO level is determined through time series analysis of the dynamic current response of the sensor cell due to load oscillations. The pattern identification algorithms are built upon the underlying concepts of *Symbolic Dynamics*, *Information Theory* and *Probabilistic Finite State Machines*. The effect of temperature on sensitivity was analyzed, and results demonstrate the efficacy of CO sensor under different operating conditions. The sensitivity of the CO sensor can be tailored for a particular application by changing the type of catalyst, its loading and operation temperature. A similar approach is now being used to develop online sensors for a variety of other important fuel cell phenomena, such as flooding and catalyst degradation.

© 2008 Elsevier B.V. All rights reserved.

1. Introduction

Polymer electrolyte fuel cells (PEFCs) are widely viewed as a promising candidate for future portable, stationary and automotive applications [1]. In a PEFC, hydrogen and oxygen react electrochemically to produce electricity, water and heat. PEFCs can be operated with neat hydrogen or with hydrogen generated by reformation of organic chemicals such as ethanol, methanol and natural gas. Due to lack of infrastructure for hydrogen, reformation of natural gas is an attractive option for stationary power applications. After reformation and CO cleanup, reformed gas mixtures still typically contain 10–100 ppm of CO, which is well known to reduce performance in PEFCs.

Vogel et al. [2] reported the mechanism of CO poisoning, by which CO chemisorbs on platinum (Pt) sites, inhibiting hydrogen adsorption. CO is more strongly bonded to Pt than hydrogen, and has a greater voltage potential required for oxidation than hydrogen. Carbon monoxide, even in small concentrations, is sufficient to cover nearly the entire electrode, which inhibits the reaction of hydrogen at anode. Very rapid oxidation of hydrogen occurs at remaining sites or holes in the compact monolayer of adsorbed CO. Surface coverage of CO, θ_{CO}, is a function of surface potential as well as partial pressure of CO. Polarization (voltage) loss due to CO poisoning in phosphoric acid fuel cells was studied by Dhar et al. [3,4].

It was reported that CO adsorption is strongly favored at low temperature due to higher negative value of standard entropy and standard free energy for CO adsorption. Zhang et al. [5] found that CO poisoning is aggravated with an increase in flow rate, while increased oxygen pressure reduces poisoning due to increased CO oxidation. The effect of operating temperature, pressure and relative humidity on CO poisoning can be found elsewhere in Refs. [6,7].

Lee et al. performed electrocatalysis of CO poisoning on Pt/C, PtSn/C and PtRu/C electrodes in PEFCs [8]. The best catalyst to mitigate CO poisoning was found to be a Pt/Ru combination, which is confirmed by many other studies [9–12]. Gottesfeld and Pafford [13] suggested a novel method of restoring the performance of a CO poisoned fuel cell when the feed stream containing a maximum of 500 ppm of CO was injected with 2–5% oxygen, thus providing an oxidative surface environment for CO oxidation reaction. This mitigative approach is known as air bleeding, but is parasitic and

* Corresponding author. Tel: +1 814 865 0060; fax +1 814 863 4848.
E-mail address: mmm124@psu.edu (M.M. Mench).

reduces overall performance. For air bleeding to be efficient, precise system control is needed, since CO output from reformer system is not constant, depending on operating conditions. Additionally, the moist hydrogen oxygen mixture is potentially explosive. Several other innovative methods for the mitigation of CO poisoning has been proposed in the literature [14–16].

Springer et al. [17] described a mathematical model of CO poisoning for calculation of CO and hydrogen coverage on the anode of a fuel cell. It was shown that even a small increase in the rate of CO oxidation could have large impact in lowering the polarization losses. Baschuk et al. reviewed CO poisoning literature for different CO poisoning modeling approaches and mitigative methods [18]. They reported the lack of consideration of transport phenomena and the effect of oxygen cross-over in existing PEFC models. A non-isothermal, multidimensional mathematical model with CO poisoning effects was developed by Baschuk et al. [19] by application of conservation laws to the diffusion media, catalyst layer and polymer electrolyte. The CO electro-oxidation rate was found to be negligible at low surface potential. At higher surface potential, current density was observed to increase due to increased electro-oxidation of CO.

Due to the current unavailability of real-time accurate mathematical models, several techniques have been reported in literature for the measurement of CO and are summarized in Table 1. These techniques include infrared absorption, sintered tin oxide, electrochemical, copper chloride and dynamic response sensors [20]. Infrared sensors [21,22] based on absorption spectroscopy are highly accurate to the ppm level but they are voluminous and hence not suitable for portable fuel cell applications. They also have large cost attached to them due to the use of infrared source and detector. Tin oxide sensors measure the change in the resistance after reduction of CO, as a measure of CO level. They consume high power due to heating requirements to maintain the operating temperature around 300 °C, but they are cross-sensitive to hydrogen. Electrochemical sensors [20,23,24] are generally amperometric, in which the signal comes from the measurement of the current produced by the electrochemical oxidation of carbon monoxide. The price of electrochemical sensors is low and they have compact and reliable operation. However, they are cross-sensitive to the hydrogen and hence cannot be used with reformate gas. Another chemi-resistance based CO sensor using copper chloride film was developed by Holt et al. [25] for measuring CO level in reformate streams. But it is cross-sensitive to H_2O and cannot be used for reformate applications, as reformate typically contains 10% moisture. Sensors based on analysis of dynamic current response have been recently suggested in literature [26–28] that are compact, low cost sensors, and can even be used in a hydrogen containing environment. However, the limitation of these sensors is that their performance depend on the moisture content in the fuel stream.

Wal et al. [23] tested the stability of electrochemical sensors and reported that response of the electrochemical sensor deteriorates if operated over a long period with dry membrane. For stable operation it was necessary to operate sensor with a water reservoir. In another approach, Kirby et al. [26] proposed to use pattern recognition for the reduction in current at a fixed cell potential to measure CO content. The reduction in current was obtained by cycling cell between reformate stream (poisoning) and humid air (recovery). It was observed that reduction in Pt loading from 0.1 to 0.005 mg/cm² increased CO poisoning and reduced the time to reach poisoned steady state at 50 ppm CO, from 10 min to 2 s. Further reduction in Pt loading was found to result in unstable sensor output. Mukundan et al. developed a low temperature CO sensor based on differential poisoning of electrodes [27]. Planje et al. [24] described a method for measurement of CO from the current response. A fuel cell with water reservoir at the cathode for constant humidification of membrane was used as CO sensor. The CO sensor was cycled through the measurement (0.35 V) and cleanup (1 V) mode by changing the anode voltage measured with respect to the cathode. In the measurement mode CO adsorption was allowed to occur over an 800 ms period. The value of cell current at the end of 800 ms was measured to find CO ppm level from the mathematical model. In the cleanup mode, the adsorbed CO was removed from the anode by increasing the potential applied at the anode.

In fuel cell stacks and systems, there is still an urgent need for non-intrusive, robust, rapid, compact and inexpensive sensors to enable both stable performance and extended lifetime operation of stack. Achieving this goal is complicated by the desire to obtain active control with a minimal number of sensors. In a stack, a limited number of basic physical signals are available (e.g. voltage, current, temperature, and manifold pressure). The thermophysical and electrochemical processes involved are highly coupled. Further, it is impractical to apply many of the diagnostic tools which are used to study single cells in a laboratory environment to a full-sized stack. With the above constraints, sensors based on analysis of current response [26–28] have been recently suggested in literature that are compact, low cost sensors, and can even be used in a hydrogen containing environment.

Along this line, this paper reports development and experimental validation of a dynamic current response sensor based on a novel pattern identification tool, called symbolic dynamic filtering (SDF) [29] for measurement of CO in the fuel stream [28]. SDF-based pattern recognition algorithms have been experimentally validated for real-time execution in different applications, such as electronic circuits [30] and fatigue damage monitoring in polycrystalline alloys [31,32]. It has been shown that SDF yields superior performance in terms of early detection of anomalies and robustness to measurement noise by comparison with other existing techniques such as Principal Component Analysis (PCA) and Artificial Neural Networks (ANN) [30,31]. The proposed CO sensor based on SDF analysis of dynamic current response can be used to determine the control strategy for the reformer output. It will provide feedback for air bleeding to determine the amount of air in the reformate for controlling sporadic overshoots in the CO level. It can also provide feedback to control the output level of the reformer. The sensor is not cross-sensitive to hydrogen in the reformate.

This paper presents development of a CO sensor for fuel cell applications and demonstrates the efficacy of symbolic dynamic filtering method for CO sensing. In this paper, the operation of CO sensor was validated in an experimental setup of an electrochemical system using certified hydrogen gas bottles premixed with carbon monoxide. Analysis of the effect of change in operation temperature on the sensitivity of the developed CO sensor is presented.

2. Operating principle of the developed CO sensor

This section presents the operating principle of the developed online CO sensing method in polymer electrolyte fuel cells. For most commercial applications and compact design, a fuel cell stack of several single cells connected in series is utilized [1]. In a fuel cell stack in series, the total current is same for each cell and is proportional to active area of each cell. Fig. 1 shows schematic of a PEFC stack operating on reformate. Reformate feed contains a mixture of H_2, CO_2, N_2 and typically a small level of CO. Control of humidification of PEFC stack temperature and coolant flow rate plays a major role in water management, which has a strong effect on the performance of the stack.

Fig. 2 explains the mechanism of CO poisoning at the anode of PEFC. Hydrogen and carbon monoxide present in the reformate

Table 1
Summary of CO sensing methods

Method	Physical principle	Advantages	Disadvantages	References
Infrared absorption	Absorption spectroscopy	High accuracy, rapid response	High cost, large system	[21,22]
Tin oxide	Chemi-resistance	Compact, low cost, rapid response	High power consumption, cross-sensitive to H_2	
Electrochemical	Amperometry	Compact, low cost, rapid response	Cross-sensitive to H_2, freezes if water reservoir used, unstable with dry membrane	[20,23,24]
Dynamic response	Pattern recognition	Low cost, tolerant with H_2	Fixed value of RH	[26–28]
Copper chloride	Chemi-resistance	Rapid response, tolerant with H_2	Cross-sensitive to H_2O	[25]

diffuse through the porous gas diffusion layer (GDL) before reaching the anode catalyst layer. Carbon monoxide forms a stronger adsorption bond and covers large fraction of electrode surface thus creating a compact monolayer. The adsorption of hydrogen occurs at the remaining sites left unoccupied by CO, which is followed by the rapid hydrogen oxidation reaction. However, voltage potential generated due to the hydrogen oxidation reaction is not sufficient to oxidize CO. If the anode over-potential is greater than 0.4 V, CO oxidation occurs at a higher rate, creating more sites for H_2 oxidation.

The behavior of a complex dynamical system, such as a fuel cell stack, can change due to the development of small anomalies (e.g., CO poisoning). In this regard, *the anomaly in a dynamical system can be defined as deviation from the nominal condition that is viewed as the desired, healthy behavior*. As discussed in the previous section, it is often difficult to rely on physics based modeling for identification of behavioral patterns in complex system, because of the inability to develop models with requisite accuracy and precision. Hence the problem of identification of statistical patterns, which constitutes the dynamical characteristics of the system, can be formulated in terms of observation based estimation of the process variables. In absence of a feasible mathematical model, the inherent dynamics (nominal or anomalous) of a complex system can be inferred from time series data generated from sensing devices that are capable of capturing the essential details of the system.

Therefore, a CO sensor has been developed for online monitoring of the CO content in the reformate stream of a fuel cell stack. The CO sensor as shown in Fig. 1 is actually a single 5 cm^2 fuel cell with 0.4 mg/cm^2 Pt loading on both cathode and anode (for details please refer to Section 3). This sensor operates on a humidified reformate hydrogen and air stream diverted from the main fuel cell stack. Due to the presence of CO in the reformate stream, the sensor is poisoned and reaches a steady state at a constant cell temperature, humidity and flow rate. A drop rate of 0.2 mA/cm^2/min in the cell current density, is considered as an indication of steady state. In this poisoned condition, the steady state current response of the sensor is monitored under an external excitation of voltage pulses for the purpose of CO sensing. The current response is recorded in terms of time series data and analyzed using the pattern identification algorithms based on symbolic dynamic filtering.

Symbolic dynamic filtering (SDF) includes preprocessing of time series data using the wavelet analysis [33], which is well suited for time-frequency analysis of non-stationary signals and enables noise attenuation and reduction of spurious disturbances from the
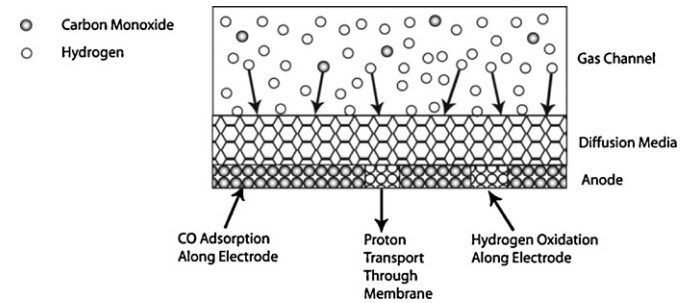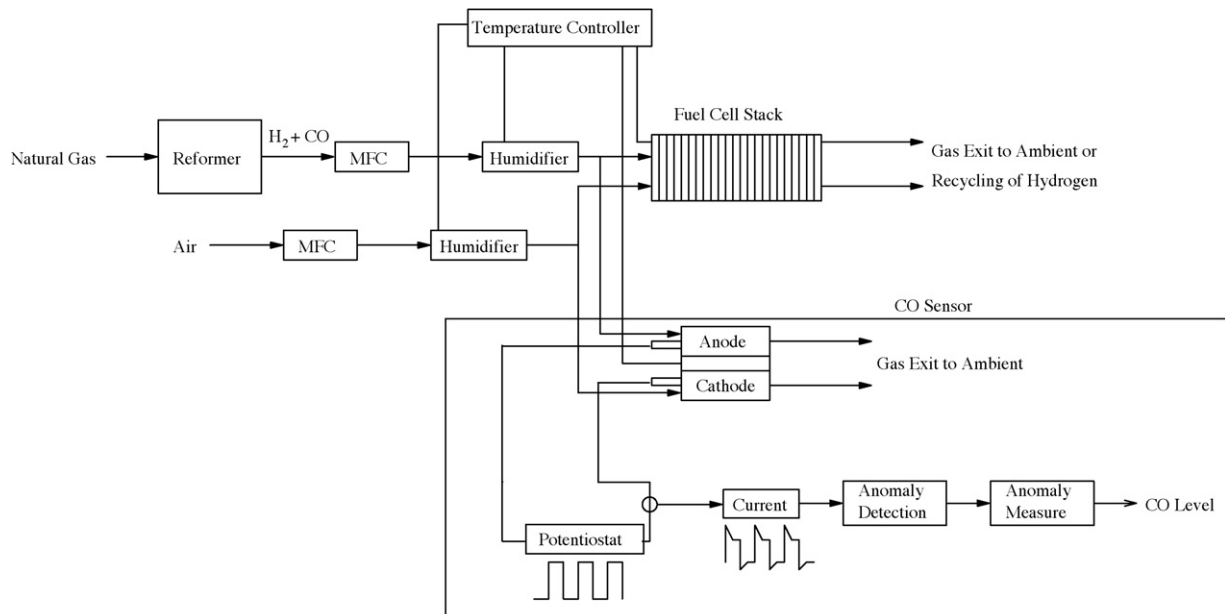

Fig. 2. CO poisoned anode of PEFC.

Fig. 1. CO sensor based on SDF.

raw time series data without any significant loss of pertinent information [34]. The wavelet-transformed data is partitioned using the *maximum entropy principle* [34] to generate the symbol sequences. Subsequently, statistical patterns of evolving anomalies are identified from these symbolic sequences through construction of a (probabilistic) finite-state machine [29] that captures the system behavior by means of information compression. The state probability vectors, which are derived from the respective state transition probability matrices of the finite state machine under the nominal and anomalous conditions, yield the statistical patterns of the evolving anomalies.

These algorithms analyze the time series data of current response of the fuel cell sensor and generate pattern vectors that are the probability distributions of the states of a finite state machine (for details please refer to Appendix A). In this procedure, the pattern vectors are generated from the current response of the sensor at the nominal condition, i.e., 0 ppm CO, and from the corresponding current response at different anomalous conditions, i.e., CO > 0 ppm. The statistical deviation of these pattern vectors from the nominal condition, is termed as anomaly measure that is an indicator of the CO level in the feed stream as it measures the deviation of system from healthy to an anomalous condition. Calibration of the sensor is required prior to measurement of CO using this dynamic system response approach. The details of implementation of the CO sensor in a fuel cell stack are provided in Section 3. The following sections clarify these concepts by providing the necessary details.

3. Experimental validation of the concept

In order to validate the concept of CO sensing in a fuel cell stack system based on symbolic dynamic filtering, a set of experiments were performed on the laboratory protocol of a single small CO sensor.

3.1. Experimental setup

Experiments were performed using a 850C fuel cell test station (Scribner Associates Inc.) and a cell with active area of 5 cm^2 with serpentine channels. A commercially available 5 cm^2 membrane electrode assembly (MEA) with Pt loading of 0.4 mg/cm^2 was used in the cell. The MEA and SGL 10 BB series gas diffusion layer, were compressed in the cell. Both air and hydrogen streams were humidified by passing the dry gases through the separate humidifiers. Anode and cathode humidifier temperatures were controlled to meet a specific relative humidity value at the cell operating temperature.
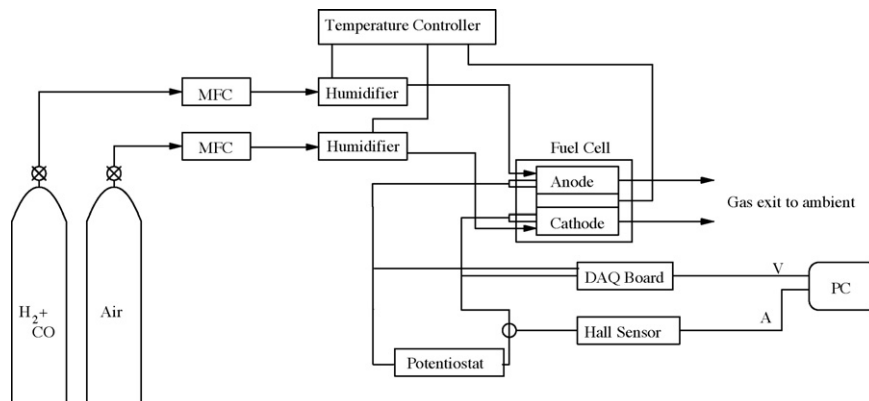

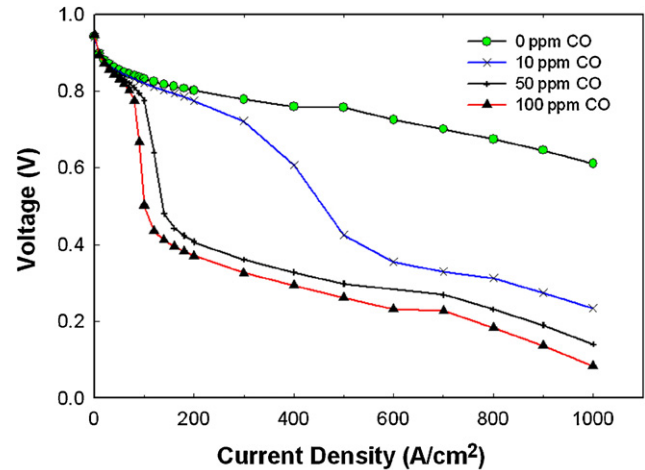**Fig. 4.** Polarization curves at 0, 10, 50, 100 ppm CO at 65 °C.

Fig. 3 shows the experimental arrangement used in the validation of the sensor. As described earlier, the CO sensor is actually a single 5 cm^2 fuel cell with 0.4 mg/cm^2 Pt loading on both cathode and anode. The cell temperature was kept constant during the entire set of experiments. For nominal case, ultra high purity hydrogen was used and experiments were performed with this pure hydrogen. For anomalous cases, i.e., with hydrogen containing CO, certified hydrogen gas bottles with premixed CO, supplied by GTS Inc. were used. Flow rates were controlled with calibrated mass flow controllers.

In these experiments, the sensor is poisoned for anomalous cases and reaches a steady state at a constant cell temperature, humidity and flow rate. A drop rate less than 0.2 mA/cm^2/min in current density was considered as a criterion to indicate attainment of steady state. Once the steady state is reached, the CO sensor is excited with an external excitation of voltage pulses and the corresponding current response of the sensor is measured for the purpose of CO sensing. In order to generate input voltage pulses for exciting the CO sensor, a circuit with potentiostats to control the sensor voltage was used. A time delay relay was used to switch the load on the sensor between two limits and thus controlling the pulse time for which it maintains the cell voltage at 0.65 and 0.45 V (see Section 3.2 for further details). Current response was measured using a Hall sensor. The current and voltage signal were passed to IOtech Inc. data acquisition (DAQ) system. Using this procedure the current response in terms of time series data was generated at the nominal condition (i.e., CO = 0 ppm) and also at different

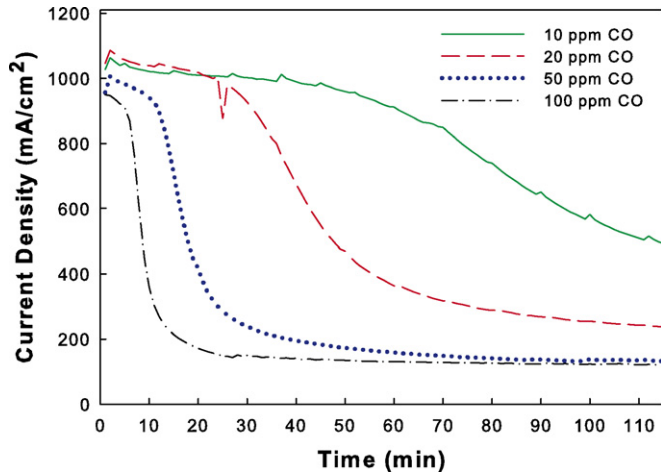**Fig. 3.** Schematic of the experimental test setup.

Fig. 5. Current density vs. time at a fixed cell voltage of 0.6 V and 65 °C.

Fig. 7. Current response of the fuel cell to the voltage pulse at 65 °C for 0, 5 and 10 ppm CO.

anomalous conditions (i.e., CO > 0 ppm). These time series data sets of the current response were analyzed using the pattern identification algorithms based on symbolic dynamic filtering.

3.2. Measurement and data analysis

In all experiments, the anode stoichiometry was set to 2 and that of cathode was set to 3 at a current density of 1 A/cm², so therefore represents a constant flow rate condition. During the experiment, the cell temperature was maintained at 65 °C. Humidification temperatures were maintained such that RH at anode and cathode were 88% and 100% RH, respectively.

The polarization curves and transient current density curves are presented here to illustrate the effect of CO poisoning on fuel cell performance and to verify the experimental test setup. The polarization curves in Fig. 4 indicate the expected drop in performance with increasing CO level. Polarization curves were obtained by using a current scan method with a time period of 1 min at each step, which allowed for stabilization of cell after the load was changed. Finer steps were used in the initial low current density region marked by steep changes. It can be inferred from the polarization curves that largest drop of 60% in power occurs at 10 ppm level at 0.61 V, followed by a further drop at 50 and 100 ppm level. For the platinum loading used (0.4 mg/cm²), the sensor reaches saturation above 100 ppm of CO.
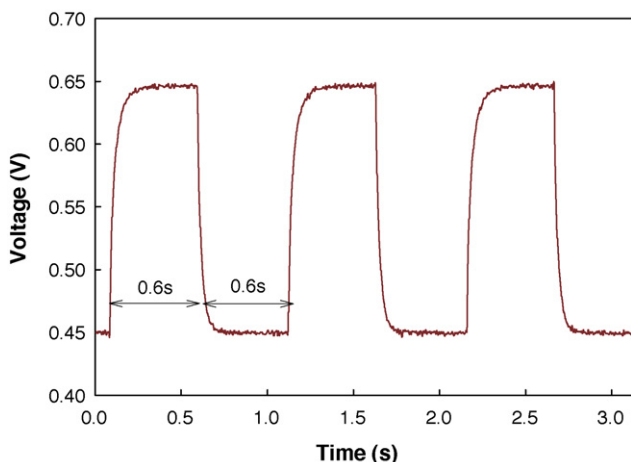
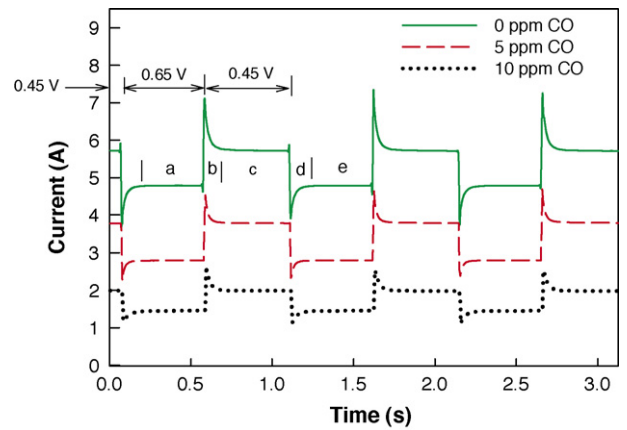At each ppm level, the fuel cell was poisoned completely before subjecting it to voltage pulsations for recording the current response. Fig. 5 shows the transient response of the fuel cell at a fixed cell voltage of 0.6 V. The time required to reach a completely poisoned steady state is a function of catalyst loading, CO level and temperature of operation. At a CO level below 10 ppm, a large time (>5 h) is required to achieve a steady state.

In order to generate the time series data of current response for each CO level, it is necessary to perturb the fuel cell system using a voltage pulse when fuel cell reaches a poisoned steady state. During poisoning, the cell voltage was maintained constant at 0.6 V. Once the cell reached steady state, it was excited with an input voltage pulse which varies cell potential cyclically from 0.65 to 0.45 V with a period of 1.2 s using rheostats and a time delay relay switch. Fig. 6 shows the voltage pulse used in the experiments. The input voltage excitation was the same for the different CO levels as well as for the healthy (i.e. pure H_2 or 0 ppm CO) system. The step change in voltage from 0.65 to 0.45 V increases the anode overpotential and accelerates the CO oxidation reaction. However, CO poisoning is a dynamic phenomena in which both adsorption and desorption occur simultaneously. When the applied cell voltage is 0.45 V, CO poisoning is still occurring along with removal of CO by oxidation. Consequently, the current at 0.45 V for a poisoned cell is lower than that for an un-poisoned cell.

During data acquisition, a sampling frequency of 200 Hz was used. A time series containing a total of 10 000 data points was
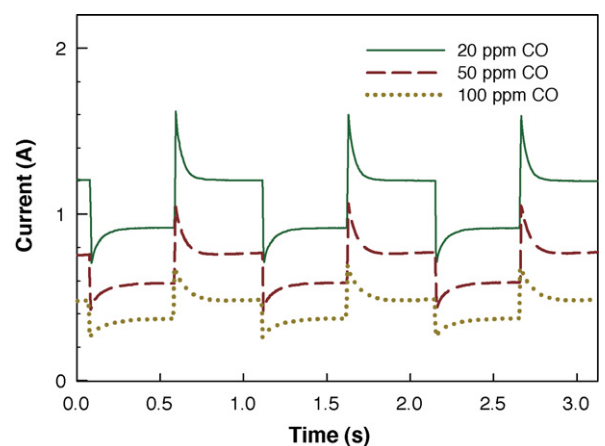

Fig. 6. Voltage pulse applied to the fuel cell.

Fig. 8. Current response of the fuel cell for the voltage pulse at 65 °C for 20, 50 and 100 ppm CO.
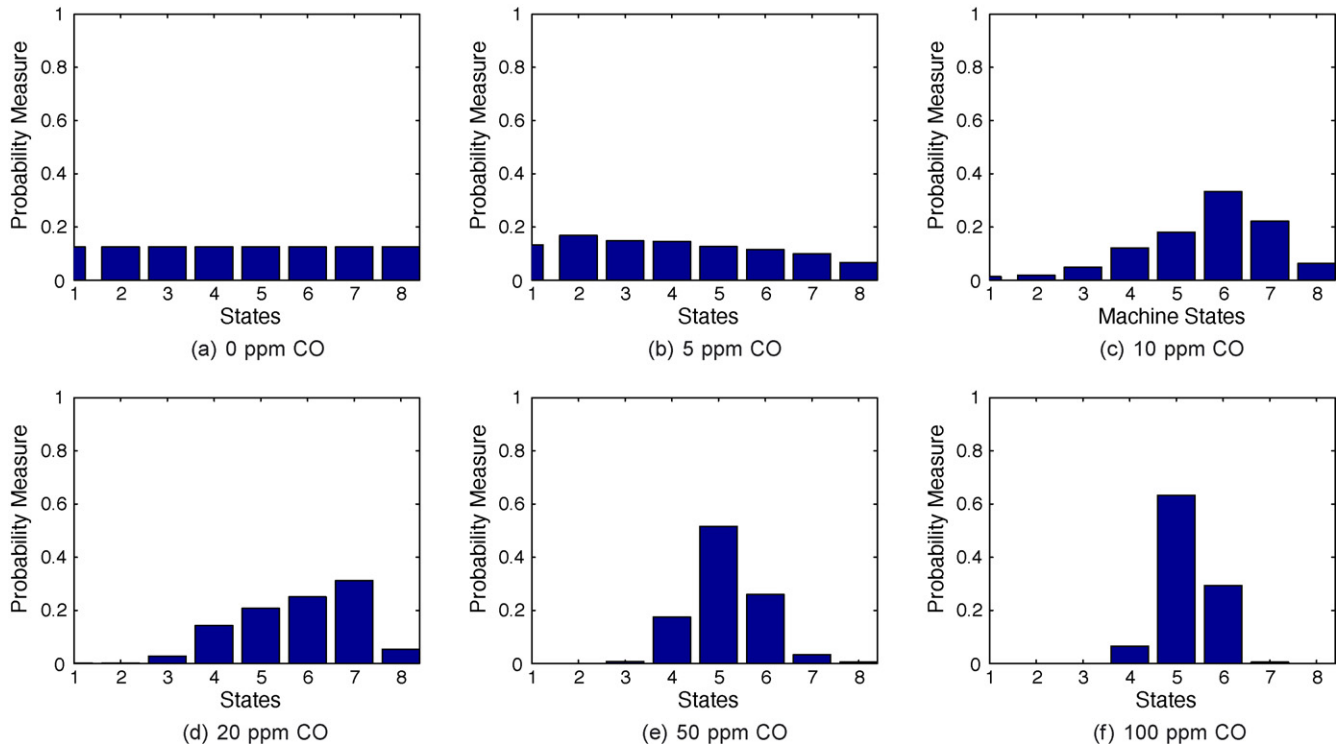
Fig. 9. Probability measure plot at 65 °C for 0, 5, 10, 20, 50 and 100 ppm CO.

collected over 50 cycles. The number of data points are governed by a stopping rule [35], which is required to find a lower bound on the length of the symbol sequence. Sampling frequency and pulse time were optimized for minimal sensing time to generate a sufficient length of data. The time series data were further analyzed using the symbolic dynamic filtering method (Appendix A) to detect the anomaly measure at each CO level. After each experiment, the poisoned membrane was recovered by passing a pure hydrogen stream for 2 h. Recovery was confirmed by comparing the polarization curves obtained after recovery and the one obtained with pure hydrogen.

The dynamic current response of the cell under voltage excitation for 0, 5 and 10 ppm CO levels is shown in Fig. 7. With

increased CO ppm in the feed stream, the poisoning effect increases, which leads to a drop in the fuel cell current. When the voltage was reduced from 0.65 to 0.45 V, an overshoot in the current was observed as shown in Region b of Fig. 7. This overshoot was due to an initially higher transient oxygen concentration present in the catalyst layer, in Region a. Overshoot in the current asymptotes to a steady value corresponding to the CO level in the feed stream as shown in Region c. In this region, cell voltage was 0.45 V, and current density is a function of CO content.

When the cell voltage was restored to 0.65 from 0.45 V, an undershoot, shown by Region d, in the current was observed because of the initially lower oxygen concentration in Region c. The lower oxygen concentration originates from the higher current density at 0.45 V. Current increased to a steady value with a further increase
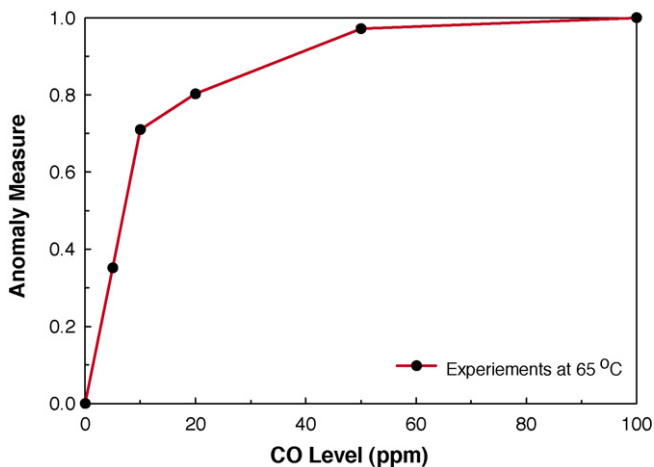

Fig. 10. Normalized anomaly measure plot at 65 °C for 0, 5, 10, 20, 50 and 100 ppm CO.
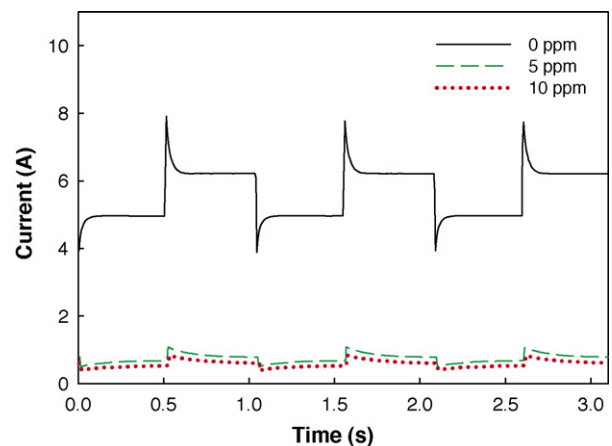

Fig. 11. Current response of the proposed CO sensor to the voltage pulse at 27 °C for 0, 5 and 10 ppm CO.
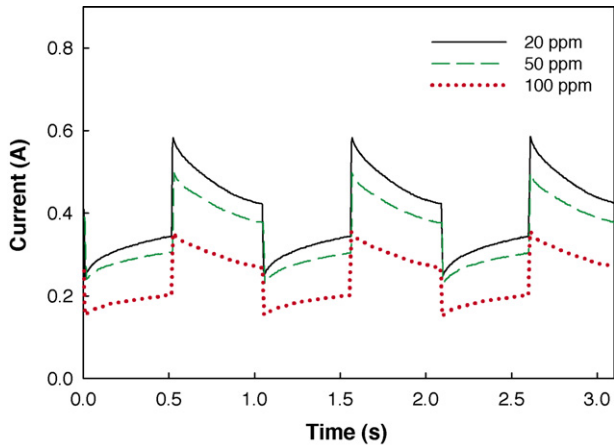
Fig. 12. Current response of the proposed CO sensor to the voltage pulse at 27 °C for 20, 50 and 100 ppm CO.

in the oxygen concentration, as shown in Region e. Fig. 8 shows the current response of the fuel cell under same voltage excitation for 20, 50 and 100 ppm CO level at 65 °C. Notice that at a given temperature of operation, the response pattern at lower ppm level is different from the one obtained at higher ppm level. It is therefore appropriate to use a pattern recognition method to identify the CO level based on the changes in the current density.

3.3. Pattern recognition using symbolic dynamics

Time series data sets of current density obtained by the voltage pulse excitation of the fuel cell at the nominal and different anomalous conditions were analyzed using the symbolic dynamic filtering algorithms for CO sensing as described in Appendix A. The nominal

condition, i.e., 0 ppm CO, was set as a reference for data analysis at different anomalous conditions. As described in Appendix A, the nominal data was analyzed using wavelet based maximum entropy partitioning scheme to generate the symbol sequence. The partition segments are not equal in size; however, all symbols have equal probability under nominal condition as a consequence of maximum entropy partitioning. Subsequently, a finite state machine was constructed using alphabet size $|\Sigma| = 8$ and window length $D = 1$. Thus total number of PFSM states are $n = |\Sigma|^D = 8$. With this selection of parameters, the PFSM yields very fast computation and low memory requirements and the algorithm was capable of sensing CO content at different anomalous conditions. The symbol sequence was passed through the finite state machine to generate the nominal state probability vector **q**. (Note: The partitioning structure and the finite state machine generated at the nominal condition, i.e. zero ppm CO, serves as the reference frame for data analysis at subsequent anomalous conditions.)

Time series data for anomalous conditions, i.e., CO > 0 ppm, were analyzed and converted to the corresponding symbol sequences using the partitioning generated at the nominal condition. These symbol sequences were then passed to the finite state machine constructed at the nominal condition to generate the corresponding state probability vectors, such that the probability vector **p** was calculated for each CO level. The statistical distance (Euclidean norm in this case) between the probability vectors of the healthy system with pure hydrogen and an anomalous system with CO > 0 ppm gives the anomaly measure value at that particular CO level (see Eq. (A.8)).

4. Results and discussion

Histograms in Fig. 9 show change in the state probability vectors due to increasing CO level for the operating temperature of 65 °C. At the nominal condition (pure hydrogen) there was a uniform dis-
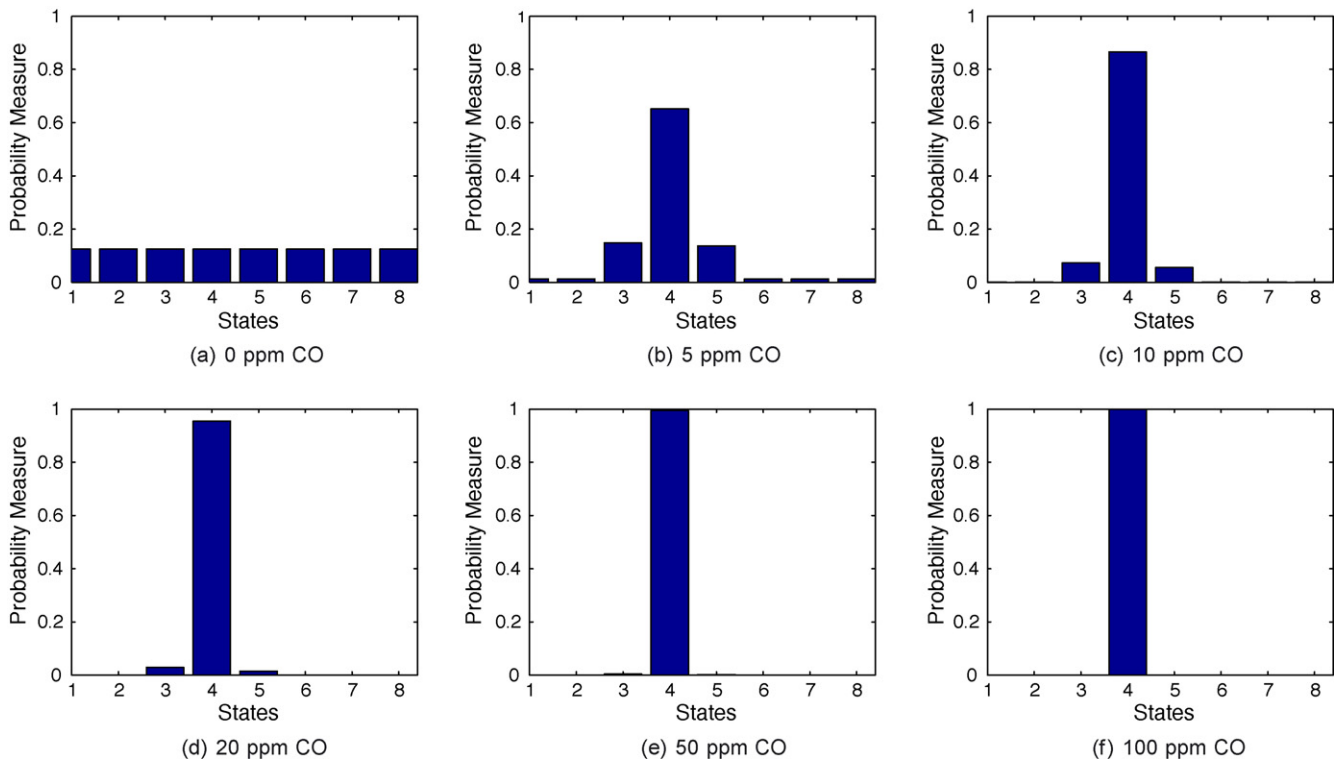

Fig. 13. Probability measure plot at 27 °C for 0, 5, 10, 20, 50 and 100 ppm CO.
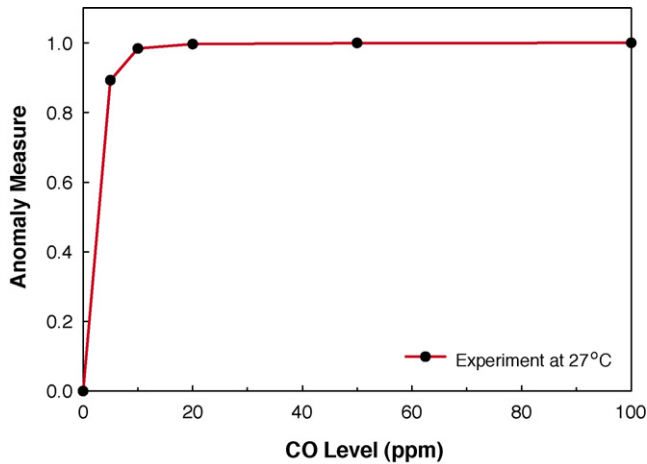
Fig. 14. Normalized anomaly plot at 27 °C for 0, 5, 10, 20, 50 and 100 ppm CO.
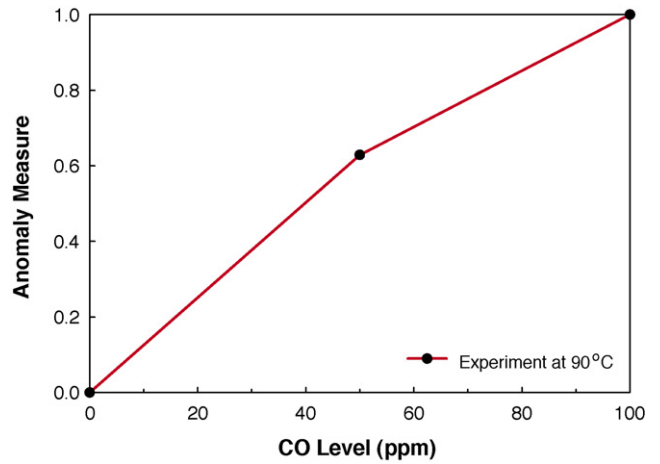

Fig. 17. Normalized anomaly plot at 90 °C for 0, 50 and 100 ppm CO.

tribution of probability among the states, as a consequence of the maximum entropy partitioning. As the anomaly level, i.e., CO content, in the system increased, the probability distribution changed from the nominal condition which fundamentally indicates the dynamic response characteristic of the CO level. Therefore, different anomalous conditions are represented by different probability distributions as shown in the histograms in Fig. 9.
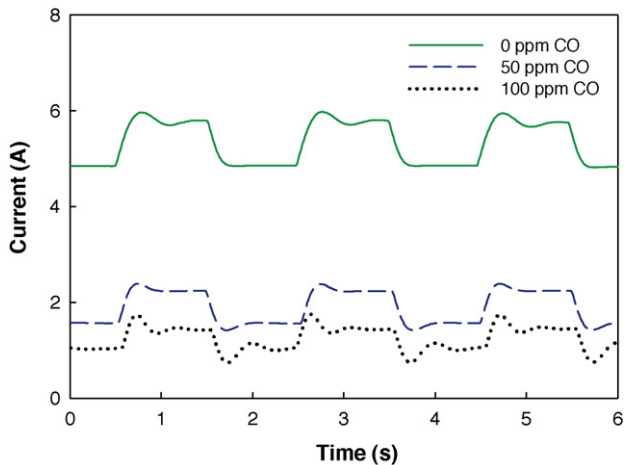

Fig. 15. Current response of the proposed CO sensor to the voltage pulse at 90 °C for 0, 50 and 100 ppm CO.

Fig. 10 shows the normalized anomaly measure plot for different CO levels for the operating temperature of 65 °C. A large increase in the anomaly measure occurs as system moves from 0 to 10 ppm CO. Further increase in the CO level results in a more subtle drop in the performance and hence anomaly curve asymptotes beyond 10 ppm, which corresponds to a CO saturated catalyst layer. A large drop in the system performance is associated with a large anomaly measure in the system. The maximum value of anomaly measure (e.g. the maximum value of CO level detectable) can be adjusted by changing the system catalyst loading, type, or temperature [28].

The anomaly measure curve obtained in Fig. 10 has key importance in the calibration of the CO sensor. It can be used for measuring the CO level when the sensor is fed with the hydrogen stream containing an unknown CO level (i.e., the inverse problem). In the inverse problem, the anomaly measure is calculated from the sensor response for the unknown CO level. From the anomaly measure in the system, we can calculate the unknown CO level using the interpolation from the anomaly measure plot. However, detailed statistical analysis of the inverse problem in presence of uncertainties is still an area of active research and is currently under investigation [32]. This work would be reported in future publications.

4.1. Effect of operating temperature

CO poisoning is strongly affected by temperature, as temperature of operation affects the rate of adsorption and desorption of CO on the anode of the sensor. CO adsorption is strongly favored at room temperature, but CO sticking reduces with increasing
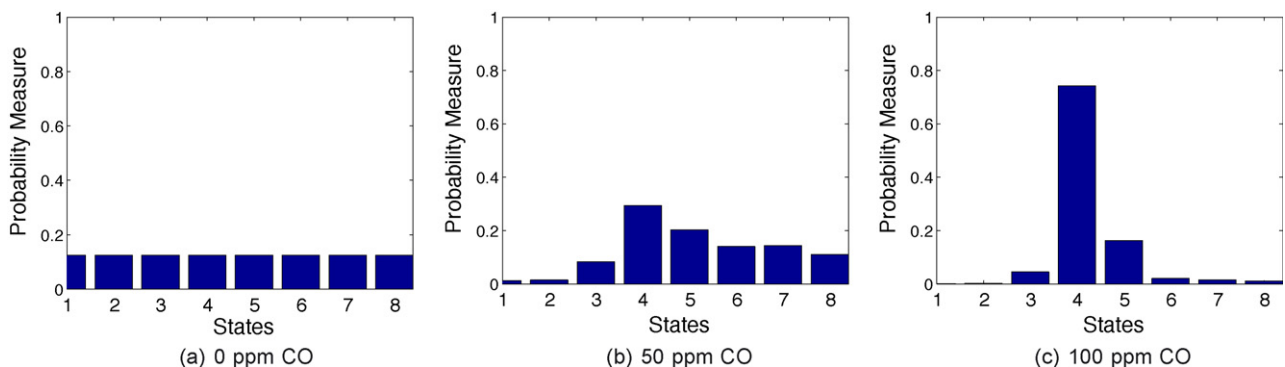

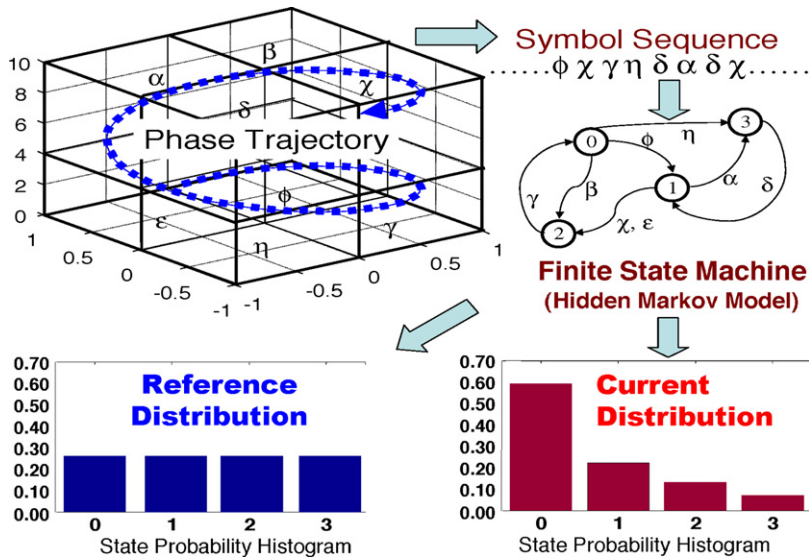**Fig. 16.** Probability measure plot at 90 °C for 0, 50 and 100 ppm CO.

Fig. 18. Concept of symbolic dynamic filtering for pattern identification.

temperature. The temperature of operation thus changes the sensitivity of the sensor, particularly at higher CO levels, where the cell saturates beyond 100 ppm CO.

Fig. 11 shows the response of the fuel cell for 0–10 ppm CO at 27 °C to the voltage pulse that was similar to the other experiment at 65 °. The response of the sensor to the voltage pulse for 20–100 ppm CO level at 27 °C is shown in Fig. 12. From these figures, it is clear that the sensor output is saturated for any CO level above 5 ppm at room temperature. Thus, room temperature operation with the tested catalyst loading can be used for a highly sensitive sensor in the low ppm range.

This is also reflected in the probability plot shown in Fig. 13, where system moves from uniform probability distribution for all states at nominal condition to almost a delta distribution at a single state for anomalous conditions beyond 5 ppm CO. Fig. 14 shows the normalized anomaly plot obtained after calculation of anomaly measure from the probability measures at 27 °C. As mentioned earlier, at room temperature, the anode catalyst becomes saturated with CO at low levels. Thus, the anomaly plot asymptotes almost after the 5 ppm level. Beyond 10 ppm CO, there is practically no difference between the anomaly measure.

In another experiment, designed to increase the range of CO sensitivity, the cell temperature was raised to 90 °C. At this higher

temperature CO sticking on the catalyst is reduced, which leads to reduction in the CO poisoning effect. An automatic voltage controller was used to generate the voltage pulses as described before. The time period of voltage pulse was increased to 2 s in order to be sufficient for the voltage controller to bring the cell voltage to the set value. The experiment at an elevated temperature was intended to study the sensitivity between 50 and 100 ppm CO and hence it was carried out for these two CO levels only.

Fig. 15 shows the response of the sensor for the voltage pulse (0.65–0.45 V), described in earlier section. Peaks in current response due to gas transport limitations are found to be reduced due to the increased vapor pressure at 90 °C, which reduces the oxygen mole fraction.

Fig. 16 shows the probability distribution plot at 90 °C, for 0–100 ppm CO range. The probability distribution at 50 ppm CO level is much different from the 100 ppm CO level. The normalized anomaly plot obtained after pulsating the cell voltage is shown in Fig. 17. Increased differential current between 50 and 100 ppm CO level, reflects the increased sensitivity between the two CO levels. Lower anomaly measure will be obtained at ppm levels below 50 ppm, which was not shown here.

It should be noted that due to the relatively simplistic nature of fuel cell response, peak-to-peak data or other correlations can also be used to achieve similar results predictive of CO levels. However the development of a CO sensor based on this approach is more robust than some other approaches and serves to demonstrate the possibilities of its use for more complex, longstanding electrochemical system sensing issues such as life time degradation.
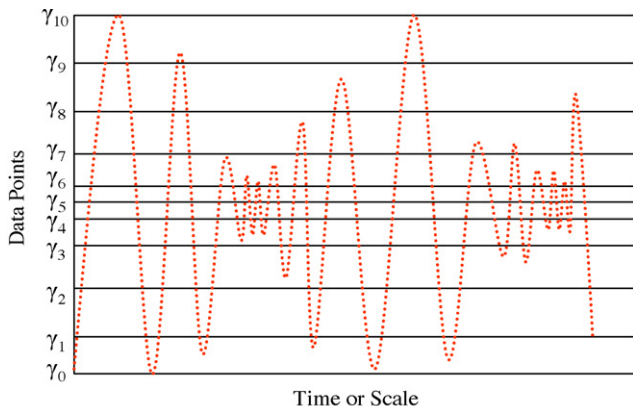

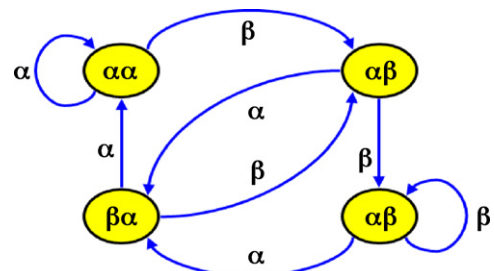**Fig. 19.** An example of maximum entropy partitioning.

Fig. 20. Example of Finite State Machine with $D = 2$ and $\Sigma = \{\alpha, \beta\}$.

Ongoing efforts at Penn State Fuel Cell Dynamics and Diagnostics Lab (FCDDL) are aimed at development of other sensors for online health monitoring of fuel cell stacks.

5. Conclusions and future work

This paper presents formulation and experimental validation of a CO sensor system for fuel cells based on an anomaly detection technique. The underlying algorithms are built upon a data-driven pattern identification tool, called symbolic dynamic filtering (SDF) [29]. The CO sensor will be useful in the fuel cell application where the feed stream is reformate with traces of CO. The response of the sensor to a step change in voltage was used to generate the dynamic current response data that is analyzed using SDF to generate statistical patterns for nominal and anomalous conditions. The difference between these patterns provide an indication of the CO content in the reformate stream and appropriate mitigative strategy can be employed.

Such a sensor is non-intrusive and offers a robust method of measurement. It can be made into a small, easily replicable and inexpensive component. Unlike electro-chemical sensors it does not have cross-sensitivity to hydrogen. It can have tailored measurement range for a given CO levels, by changing catalyst type, catalyst loading and temperature of operation. Increased temperature of operation results in a higher maximum CO levels sensing range, whereas a room temperature sensor can be used with high sensitivity in the extremely low ppm range. After calibration it can be used in the dilute hydrogen streams.

It should be noted that an alternate approach based on normalization of current values could also be used for calibration of the sensor. However, the purpose of this investigation is to develop and demonstrate a method of CO sensing in electrochemical systems based on dynamic response of the sensor. This method of sensing gradually evolving anomalies in the system is now being extended to identify several other important phenomena like flooding and catalyst degradation.

At present the sensing time for CO measurement is on the order of a few minutes, due to the time required to reach the steady state for the $5\,cm^2$ cell at $0.4\,mg/cm^2$ Pt loading. Use of Pt loading as small as $0.005\,mg/cm^2$ and much smaller surface area electrode can reduce the time required to reach steady state to around a second. All of the data acquisition, pulsing and anomaly calculation can be embedded into a compact rapid response sensor for practical application.

Appendix A. Symbolic dynamic filtering concept

This section presents a brief summary of the underlying concepts and essential features of a recently reported data-driven pattern identification tool called symbolic dynamic filtering (SDF) [29]. The concept of SDF is built upon the principles of several disciplines including *Symbolic Dynamics* [36,37], *Statistical Pattern Recognition* [38], *Information Theory* [39] and *Probabilistic Finite State Machines* [40].

While the details are reported in recent publications [29,41,34], the essential concepts of space partitioning, symbol sequence generation, construction of a finite-state machine from the generated symbol sequence and pattern recognition are consolidated here and

succinctly described for self-sufficiency, completeness and clarity of the paper. Fig. 18 exemplifies the partitioning of the phase space where each block is assigned a particular symbol such that a symbol sequence is generated from the phase space at a given time epoch. Once the symbol sequence is obtained, the next step is construction of a finite state machine [40] and generation of state probability vectors for pattern identification. These steps are described below.

A.1. Symbolic dynamic encoding

This subsection briefly describes the concepts of *Symbolic Dynamics* for:

1. Encoding nonlinear system dynamics from observed time series data for generation of symbol sequences, and
2. Construction of a probabilistic finite state machine (PFSM) from symbol sequences for generation of pattern vectors as representation of the dynamical system's characteristics.

The continuously-varying finite-dimensional model of a dynamical system is usually formulated in the setting of an initial value problem as:

$$\frac{d\mathbf{x}(t)}{dt} = f(\mathbf{x}(t), \theta(t_s)); \quad \mathbf{x}(0) = \mathbf{x}_0, \tag{A.1}$$

where $t \in [0, \infty)$ denotes the (fast-scale) time; $\mathbf{x} \in \mathbb{R}^n$ is the state vector in the phase space; and $\theta \in \mathbb{R}^\ell$ is the (possibly anomalous) parameter vector varying in (slow-scale) time t_s. The gradual change in the parameter vector $\theta \in \mathbb{R}^\ell$ due to possible evolution of anomalies (for e.g., CO content in the reformate stream) can alter the system dynamics and hence change the state trajectory.

Let $\Omega \subset \mathbb{R}^n$ be a compact (i.e., closed and bounded) region, within which the trajectory of the dynamical system, governed by Eq. (A.1), is circumscribed as illustrated in Fig. 18. The region Ω is partitioned as $\{\Phi_0, \ldots, \Phi_{|\Sigma|-1}\}$ consisting of $|\Sigma|$ mutually exclusive (i.e., $\Phi_j \cap \Phi_k = \emptyset, \forall j \neq k$), and exhaustive (i.e., $\cup_{j=0}^{|\Sigma|-1} \Phi_j = \Omega$) cells, where Σ is the *symbol alphabet* that labels the partition cells. A trajectory of the dynamical system is described by the discrete time series data as: $\{\mathbf{x}_0, \mathbf{x}_1, \mathbf{x}_2, \ldots\}$, where each $\mathbf{x}_i \in \Omega$. The trajectory passes through or touches one of the cells of the partition; accordingly the corresponding symbol is assigned to each point $\mathbf{x}_i$ of the trajectory as defined by the mapping $\mathcal{M} : \Omega \to \Sigma$. Therefore, a sequence of symbols is generated from the trajectory starting from an initial state $\mathbf{x}_0 \in \Omega$, such that:

$$\mathbf{x}_0 \longmapsto s_0 s_1 s_2 \ldots s_j \ldots \tag{A.2}$$

where $s_k \triangleq \mathcal{M}(\mathbf{x}_k)$ is the symbol generated at the (fast scale) instant k. The symbols s_k, $k = 0, 1, \ldots$ are identified by an index set $\mathcal{I}$: $\mathbb{Z} \to \{0, 1, 2, \ldots |\Sigma| - 1\}$, i.e., $\mathcal{I}(k) = i_k$ and $s_k = \sigma_{i_k}$ where $\sigma_{i_k} \in \Sigma$. Equivalently, Eq. (A.2) is expressed as:

$$\mathbf{x}_0 \longmapsto \sigma_{i_0} \sigma_{i_1} \sigma_{i_2} \ldots \sigma_{i_j} \ldots \tag{A.3}$$

The mapping in Eqs. (A.2) and (A.3) is called *Symbolic Dynamics* as it attributes a legal (i.e., physically admissible) symbol sequence to the system dynamics starting from an initial state. The partition is called a generating partition of the phase space Ω if every legal (i.e., physically admissible) symbol sequence uniquely determines a specific initial condition $\mathbf{x}_0$. In other words, every (semi-infinite) symbol sequence uniquely identifies one continuous space orbit [42].

Symbolic dynamics may also be viewed as coarse graining of the phase space, which is subjected to (possible) loss of information resulting from granular imprecision of partitioning boxes. However, the essential robust features (e.g., periodicity and chaotic behavior

of an orbit) are expected to be preserved in the symbol sequences through an appropriate partitioning of the phase space [43].

Fig. 18 pictorially elucidates the concepts of partitioning a finite region of the phase space and the mapping from the partitioned space into the symbol alphabet, where the symbols are indicated by Greek letters (e.g., α, β, γ, δ, ...). This represents a spatial and temporal discretization of the system dynamics defined by the trajectories. Fig. 18 also shows conversion of the symbol sequence into a finite-state machine and generation of the state probability vectors at the current and the reference conditions. The states of the finite state machine and the histograms in Fig. 18 are indicated by numerics (i.e., 1, 2, 3 and 4); the necessary details are provided later in Appendix A.3. Although the theory of phase-space partitioning is well developed for one-dimensional mappings [42], very few results are known for two and higher dimensional systems. Furthermore, the state trajectory of the system variables may be unknown in case of systems for which a model as in Eq. (A.1) is not known or is difficult to obtain. As such, as an alternative, the time series data set of selected observable outputs can be used for symbolic dynamic encoding as explained in the following subsection.

A.2. Wavelet space partitioning

As described earlier, a crucial step in symbolic dynamic filtering (SDF) is partitioning of the phase space for symbol sequence generation [37]. Several partitioning techniques have been reported in literature for symbol generation [44,45], primarily based on symbolic false nearest neighbors (SFNN). These techniques rely on partitioning the phase space and may become cumbersome and extremely computation-intensive if the dimension of the phase space is large. Moreover, if the time series data is noise-corrupted, then the symbolic false neighbors would rapidly grow in number and require a large symbol alphabet to capture the pertinent information on the system dynamics. Therefore, symbolic sequences as representations of the system dynamics should be generated by alternative methods because phase-space partitioning might prove to be a difficult task in the case of high dimensions and presence of noise. The wavelet transform [33] largely alleviates these shortcomings and is particularly effective with noisy data from high-dimensional dynamical systems [34]. As such, this paper has used a wavelet-based partitioning approach [29,34] for construction of symbol sequences from time series data.

In wavelet-based partitioning approach, time series data are first converted to wavelet domain, where wavelet coefficients are generated at different time shifts. The choice of the wavelet basis function and wavelet scales depends on the time-frequency characteristics of individual signals. Guidelines for selection of basis functions and scales are reported in literature [34].

The wavelet space is partitioned with alphabet size $|\Sigma|$ into segments of coefficients on the ordinate separated by horizontal lines. The choice of $|\Sigma|$ depends on specific experiments, noise level and also the available computation power. A large *alphabet* may be noise-sensitive while a small alphabet could miss the details of signal dynamics [34]. The partitioning is done such that the regions with more information are partitioned finer and those with sparse information are partitioned coarser. This is achieved by maximizing the Shannon entropy [39], which is defined as:

$$S = -\sum_{i=0}^{|\Sigma|-1} p_i \log(p_i) \tag{A.4}$$

where p_i is the probability of a data point to be in the ith partition segment. Uniform probability distribution, i.e., $p_i = (1/|\Sigma|)$ for $i = 0, 1, \ldots, |\Sigma|-1$, is a consequence of maximum entropy partitioning [34]. In the illustrative example of Fig. 19, the partitioning

contains 10 cells (i.e., line intervals in this case), where the size of the cells is smaller for regions with higher density of data points to ensures an unbiased partition such that each cell is allocated equal number of visits at the nominal condition.

Each partition segment is labelled by a symbol from the alphabet Σ and accordingly the symbol sequence is generated from the wavelet coefficients. The structure of the partition is fixed at the nominal condition, which serves as the reference frame for symbol sequence generation from time series data at anomalous condition(s).

A.3. Probabilistic finite state machine (PFSM) and pattern identification

Once the symbol sequence is obtained, the next step is the construction of a Probabilistic Finite State Machine (PFSM) and calculation of the respective state probability vector as depicted in the lower part of Fig. 18 by the histograms. The partitioning (see Fig. 19) is performed at the nominal condition that is chosen to be the healthy state having no anomalies.

A PFSM is then constructed at the nominal condition, where the states of the machine are defined corresponding to a given *alphabet* set Σ and window length D. The alphabet size $|\Sigma|$ is the total number of partition segments while the window length D is the length of consecutive symbol words [29], which are chosen as all possible words of length D from the symbol sequence. Each state belongs to an equivalence class of symbol words of length D, which is characterized by a word of length D at the leading edge. Therefore, the number n of such equivalence classes (i.e., states) is less than or equal to the total permutations of the alphabet symbols within words of length D. That is, $n \leq |\Sigma|^D$; some of the states may be forbidden, i.e., these states have zero probability of occurrence. For example, if $\Sigma = \{\alpha, \beta\}$, i.e., $|\Sigma| = 2$ and if $D = 2$, then the number of states is $n \leq |\Sigma|^D = 4$; and the possible states are words of length $D = 2$, i.e., $\alpha\alpha, \alpha\beta, \beta\alpha$, and $\beta\beta$, as shown in Fig. 20.

The choice of $|\Sigma|$ and D depends on specific applications and the noise level in the time series data as well as on the available computation power and memory availability. As stated earlier, a large *alphabet* may be noise-sensitive and a small alphabet could miss the details of signal dynamics. Similarly, while a larger value of D is more sensitive to signal distortion, it would create a much larger number of states requiring more computation power and increased length of the data sets. In the results section of this paper, the analysis of time series data sets is done using the window length equal to $D = 1$; consequently, the set of states Q is equivalent to the symbol alphabet Σ. With the selection of the parameters $D = 1$ and $|\Sigma| = 8$, the PFSM has $n = 8$ states. With this choice of parameters, the SDF algorithm is shown to be capable of detecting the CO content in the fuel cell stack experimental setup. However, other applications such as two-dimensional image processing, may require larger values of the parameter D and hence possibly larger number of states in the PFSM.

Using the symbol sequence generated from the time series data, the state machine is constructed on the principle of sliding block codes [36]. The window of length D on a symbol sequence is shifted to the right by one symbol, such that it retains the most recent $(D - 1)$ symbols of the previous state and appends it with the new symbol at the extreme right. The symbolic permutation in the current window gives rise to a new state. The PFSM constructed in this fashion is called the D-Markov machine [29], because of its Markov properties.

Definition Appendix A.1. A symbolic stationary process is called D-Markov if the probability of the next symbol depends

only on the previous D symbols, i.e., $P(s_j|s_{j-1} \ldots s_{j-D}s_{j-D-1} \ldots) = P(s_j|s_{j-1} \ldots s_{j-D})$.

The finite state machine constructed above has D-Markov properties because the probability of occurrence of symbol $\sigma \in \Sigma$ on a particular state depends only on the configuration of that state, i.e., the previous D symbols. The states of the machine are marked with the corresponding symbolic word permutation and the edges joining the states indicate the occurrence of a symbol σ. The occurrence of a symbol at a state may keep the machine in the same state or move it to a new state.

Definition Appendix A.2. Let $\varXi$ be the set of all states of the finite state machine. Then, the probability of occurrence of symbols that cause a transition from state ξ_j to state ξ_k under the mapping $\delta : \varXi \times \Sigma \to \varXi$ is defined as:

$$\pi_{jk} = P(\sigma \in \Sigma|\delta(\xi_j, \sigma) \to \xi_k); \quad \sum_k \pi_{jk} = 1; \quad (A.5)$$

Thus, for a D-Markov machine, the irreducible stochastic matrix $\mathbf{\Pi} \equiv [\pi_{ij}]$ describes all transition probabilities between states such that it has at most $|\Sigma|^{D+1}$ nonzero entries. The definition above is equivalent to an alternative representation such that,

$$\pi_{jk} \equiv P(\xi_k|\xi_j) = \frac{P(\xi_j, \xi_k)}{P(\xi_j)} = \frac{P(\sigma_{i_0} \cdots \sigma_{i_{D-1}} \sigma_{i_D})}{P(\sigma_{i_0} \cdots \sigma_{i_{D-1}})} \quad (A.6)$$

where the corresponding states are denoted by $\xi_j \equiv \sigma_{i_0} \cdots \sigma_{i_{D-1}}$ and $\xi_k \equiv \sigma_{i_1} \cdots \sigma_{i_D}$. This phenomenon is a consequence of the PFSM construction based on the principle of sliding block codes described above, where the occurrence of a new symbol causes a transition to another state or possibly the same state.

For computation of the state transition probabilities from a given symbol sequence at a particular slow time epoch, a D-block (i.e., a window of length D) is moved by counting occurrences of symbol blocks $\sigma_{i_0} \cdots \sigma_{i_{D-1}} \sigma_{i_D}$ and $\sigma_{i_0} \cdots \sigma_{i_{D-1}}$, which are respectively denoted by $N(\sigma_{i_0} \cdots \sigma_{i_{D-1}} \sigma_{i_D})$ and $N(\sigma_{i_0} \cdots \sigma_{i_{D-1}})$. Note that if $N(\sigma_{i_0} \cdots \sigma_{i_{D-1}}) = 0$, then the state $\sigma_{i_0} \cdots \sigma_{i_{D-1}} \in \varXi$ has zero probability of occurrence. For $N(\sigma_{i_0} \cdots \sigma_{i_{D-1}}) \neq 0$, the estimates of the transitions probabilities are then obtained by these frequency counts as follows:

$$\pi_{jk} \approx \frac{N(\sigma_{i_0} \cdots \sigma_{i_{D-1}} \sigma_{i_D})}{N(\sigma_{i_0} \cdots \sigma_{i_{D-1}})} \quad (A.7)$$

where the criterion for convergence of the estimated π_{jk}, is given in [41] as a stopping rule for frequency counting.

The symbol sequence generated from the time series data at the nominal condition, (i.e., CO = 0 ppm), set as a benchmark, is used to compute the *state transition matrix* $\mathbf{\Pi}$ using Eq. (A.7). The left eigenvector $\mathbf{q}$ corresponding to the unique unit eigenvalue of the irreducible stochastic matrix $\mathbf{\Pi}$ is the probability vector whose elements are the stationary probabilities of the states belonging to $\varXi$ [29]. Similarly, the state probability vector $\mathbf{p}$ is obtained from time series data at a (possibly) anomalous condition (i.e., CO > 0 ppm). The partitioning of time series data and the state machine structure should be the same in both cases but the respective state transition matrices could be different. The probability vectors $\mathbf{p}$ and $\mathbf{q}$ are estimates of the respective true probability vectors and are treated as statistical patterns.

Pattern changes may take place in dynamical systems due to progression of anomalies. The pattern changes are quantified as deviations from the nominal pattern (i.e., the probability distribution at the nominal condition). The resulting anomalies (i.e., deviations of the evolving patterns from the nominal pattern) are characterized by a scalar-valued function, called *anomaly measure*

μ. The anomaly measures are obtained as:

$$\mu \equiv d(\mathbf{p}, \mathbf{q}) \quad (A.8)$$

where the $d(\cdot, \cdot)$ is an appropriately defined distance function.

A.4. Summary of SDF-based pattern recognition

The symbolic dynamic filtering (SDF) method of statistical pattern recognition for anomaly detection is summarized below.

- Acquisition of time series data from appropriate sensor(s) variables (e.g., current response of the CO sensor) at a nominal condition (i.e., CO = 0 ppm), when the system is assumed to be in the healthy state (i.e., zero anomaly measure)
- Generation of the wavelet transform coefficients of the data obtained with an appropriate choice of the wavelet basis and scale [34]
- Maximum entropy partitioning in the wavelet domain at the nominal condition (see Appendix A.2) and generation of the corresponding symbol sequence
- Construction of the D-Markov machine and computation of the state probability vector $\mathbf{q}$ at the nominal condition
- Generation of a time series data sequence at another (possibly) anomalous condition (i.e., CO > 0 ppm) and conversion to the wavelet domain to generate the respective symbolic sequence based on the partitioning constructed at the nominal condition
- Computation of the corresponding state probability vector $\mathbf{p}$ using the finite state machine constructed at the nominal condition
- Computation of scalar *anomaly measure* μ (see Eq. (A.8)).

Capability of SDF has been demonstrated for anomaly detection at early stages of gradually evolving anomalies by real-time experimental validation. Application examples include active electronic circuits [30] and fatigue damage monitoring in polycrystalline alloys [31,32]. In this regard, major advantages of SDF are listed below:

(i) Robustness to measurement noise and spurious signals [34]
(ii) Adaptability to low-resolution sensing due to the coarse graining in space partitions [29]
(iii) Capability for small change detection because of sensitivity to signal distortion [31] and
(iv) Real-time execution on commercially available inexpensive platforms [30,31].

References

[1] M.M. Mench, Fuel Cell Engines, John Wiley & Sons, 2008.
[2] W. Vogel, J. Lundquist, P. Ross, P. Stonehart, Reaction pathways and poisons–II. The rate controlling step for electrochemical oxidation of hydrogen on Pt in acid and poisoning of the reaction by CO, Electrochim. Acta 20 (1975) 79–93.
[3] H.P. Dhar, L.G. Christner, A.K. Kush, H.C. Maru, Performance study of a fuel cell Pt-on-C anode in presence of CO and CO_2 and calculation of adsorption parameters for CO poisoning, J. Electrochem. Soc. 133 (8) (1986) 1574–1582.
[4] H.P. Dhar, L.G. Christner, A.K. Kush, Nature of CO adsorption during H_2 oxidation in relation to modelling for CO poisoning of a fuel cell anode, J. Electrochem. Soc. 134 (12) (1987) 3021–3026.
[5] J. Zhang, T. Thampan, R. Datta, Influence of anode flow rate and cathode oxygen pressure on CO poisoning of proton exchange membrane fuel cells, J. Electrochem. Soc. 149 (2002) A722–A765.
[6] M. Murthy, M. Esayian, W.-K. Lee, J.W. Van Zee, The effect of temperature and pressure on the performance of PEMFC exposed to transient CO concentration, J. Electrochem. Soc. 150 (2003) A29–A34.
[7] R. Jiang, H.R. Kunz, J.M. Fenton, Influence of temperature and relative humidity on performance and CO tolerance of PEM fuel cells with Nafion-Teflon-Zr(HPO$_4$)$_2$ higher temperature composite membranes, Electrochim. Acta (2006) 5596–5605.

[8] S.J. Lee, S. Mukerjee, E.A. Ticianelli, J. McBreen, Electrocatalysis of CO tolerance in hydrogen oxidation reaction in PEM fuel cell, Electrochim. Acta 44 (1999) 3283–3293.

[9] Z. Qi, A. Kaufman, CO tolerance of low loaded Pt/Ru anodes for PEM fuel cells, J. Power Sources 113 (2003) 115–123.

[10] H.A. Gasteiger, N. Markovic, P.N. Ross, E.J. Cairns Jr., CO electro-oxidation on well characterized Pt–Ru alloys, J. Phys. Chem. 98 (2) (1994) 617–625.

[11] F. Buatier de Mongeot, M. Scherer, B. Gleich, E. Kopatzki, R.J. Behm, CO adsorption and oxidation on bimetallic Pt/Ru(0 0 1) surfaces—a combined STM and TPD/TPR study, Surf. Sci. 411 (1998) 249–262.

[12] A. Kabbabi, J.-M. Leger, C. Lamy, In situ FTIRS study of the electrocatalytic oxidation of carbon monoxide and methanol at platinum–ruthenium bulk alloy electrodes, J. Electroanal. Chem. 444 (1998) 41–53.

[13] S. Gottesfeld, J. Pafford, A new approach to the problem of carbon monoxide poisoning in fuel cells operating at low temperatures, J. Electrochem. Soc. (1988) 2651–2652.

[14] A.T. Haug, R.E. White, J.W. Weidner, W. Huang, Development of a novel CO tolerant proton exchange membrane fuel cell anode, J. Electrochem. Soc. 149 (2002) A862–A867.

[15] R.J. Bellows, E. Marucchi-Soos, R.P. Reynolds, Mechanism of CO mitigation in proton exchange membrane fuel cells using dilute H_2O_2 in the anode humidifier, Electrochem. Solid-State Lett. 1 (1998) 69–70.

[16] C. He, H.R. Kunz, J.M. Fenton, Selective oxidation of CO in hydrogen under fuel cell operating conditions, J. Electrochem. Soc. 148 (2001) A1116–A1124.

[17] T.E. Springer, T. Rockward, T.A. Zawodzinski, S. Gottesfeld, Model for polymer electrolyte fuel cell operation on reformate feed, J. Electrochem. Soc. 148 (1) (2001) A11–A23.

[18] J.J. Baschuk, X. Li, Carbon monoxide poisoning of proton exchange membrane fuel cells, Int. J. Energy Res. 25 (2001) 695–713.

[19] J.J. Baschuk, A.M. Rowe, X. Li, Modeling and simulation of PEM fuel cells with CO poisoning, J. Energy Resour. Technol. 125 (2003) 94–100.

[20] S.B. Lee, A. Cocco, D. Keyvani, G.J. Maclay, Humidity dependence of carbon monoxide oxidation rate in a Nafion based electrochemical cell, J. Electrochem. Soc. 142 (1) (1995) 157–160.

[21] K.W. Kirby, A.C. Phelps, R.N. Schwartz, Method for improved detection of carbon monoxide by infrared absorption spectroscopy. US Patent No. 6,645,772 (2003).

[22] J.R. Gord, R.P. Lucht, T.N. Anderson, R. Barron-Jimenez, T. Walther, S. Roy, M.S. Brown, J.A. Caton, Diode-laser-based mid-infrared absorption sensor for carbon monoxide. US Patent No. 11,025,827 (2007).

[23] P.D. Van der Wal, N.F. De Rooji, M. Koudelka-Hep, Extremely stable nafion based carbon monoxide sensor, Sens. Actuators B Chem. 35 (1996) 119–123.

[24] W.G. Planje, G.J.M. Janssen, M.P. de Heer, A two-electrode sensor cell for CO detection in H_2-rich gas, Sens. Actuators B Chem. 99 (2004) 544–555.

[25] C.T. Holt, A.-M. Azad, S.L. Swartz, R.R. Rao, P.K. Dutta, Carbon monoxide sensor for PEM fuel cell systems, Sens. Actuators B Chem. 87 (2002) 414–420.

[26] K.W. Kirby, A.C. Chu, K.C. Fuller, Detection of low level carbon monoxide in hydrogen-rich gas streams, Sens. Actuators B Chem. 95 (2003) 224–231.

[27] R. Mukundan, E.L. Brosha, F.H. Garzon, A low temperature sensor for detection of carbon monoxide in hydrogen, Solid State Ionics 175 (2004) 497–501.

[28] M.M. Mench, A. Ray, S. Chin, E.C. Kumbur, Rapid-response sensor for carbon monoxide. Patent 20070166585 (2007).

[29] A. Ray, Symbolic dynamic analysis of complex systems for anomaly detection, Sig. Proc. 84 (7) (2004) 1115–1130.

[30] S. Chin, A. Ray, V. Rajagopalan, Symbolic time series analysis for anomaly detection: a comparative evaluation, Sig. Proc. 85 (9) (2005) 1859–1868.

[31] S. Gupta, A. Ray, E. Keller, Symbolic time series analysis of ultrasonic data for early detection of fatigue damage, Mech. Syst. Signal. Pr. 21 (2) (2007) 866–884.

[32] S. Gupta, A. Ray, Real-time fatigue life estimation in mechanical systems, Meas. Sci. Technol. 18 (7) (2007) 1947–1957.

[33] S. Mallat, A Wavelet Tour of Signal Processing, second ed., Academic Press, 1998.

[34] V. Rajagopalan, A. Ray, Symbolic time series analysis via wavelet-based partitioning, Sig. Proc. 86 (11) (2006) 3309–3320.

[35] S. Gupta, A. Ray, A. Mukhopadhyay, Anomaly detection in thermal pulse combustors using symbolic time series analysis, Proc. Inst. Mech. Eng. I-J. Sys. (Part I) (2006) 339–351.

[36] D. Lind, M. Marcus, An Introduction to Symbolic Dynamics and Coding, Cambridge University Press, United Kingdom, 1995.

[37] C.S. Daw, C.E.A. Finney, E.R. Tracy, A review of symbolic analysis of experimental data, Rev. Sci. Instrum. 74 (2) (2003) 915–930.

[38] R. Duda, P. Hart, D. Stork, Pattern Classification, John Wiley & Sons Inc., 2001.

[39] T.M. Cover, J.A. Thomas, Elements of Information Theory, John Wiley, New York, 1991.

[40] H.E. Hopcroft, R. Motwani, J.D. Ullman, Introduction to Automata Theory, Languages, and Computation, second ed., Addison Wesley, Boston, 2001.

[41] S. Gupta, A. Ray, Symbolic Dynamic Filtering for Data-Driven Pattern Recognition, in: E.A. Zoeller (Ed.), Pattern Recognition: Theory and Application, Nova, Science Publisher, Hauppage, NY, 2008 (Chapter 2).

[42] C. Beck, F. Schlogl, Thermodynamics of Chaotic Systems: An Introduction, Cambridge University Press, United Kingdom, 1993.

[43] R. Badii, A. Politi, Complexity hierarchical structures and scaling in physics, Cambridge University Press, United Kingdom, 1997.

[44] H. Kantz, T. Schreiber, Nonlinear Time Series Analysis, second ed., Cambridge University Press, Cambridge, U.K, 2004.

[45] M.B. Kennel, M. Buhl, Estimating good discrete partitions form observed data: symbolic false nearest neighbors, Phys. Rev. E 91 (8) (2003) 084102.

Biographies

Kamalesh Bhambare will obtain his MS in Mechanical Engineering from Penn State University in August 2008. His research interests include computational modeling of low temperature fuel cells and the development of sensors for fuel cell systems.

Shalabh Gupta obtained his Phd. in Mechanical Engineering from Pennsylvania State University, University Park, PA, in year 2006. He also received two master of science degrees one in Mechanical engineering and the other in Electrical engineering both from Pennsylvania State University. Dr. Gupta is currently a research associate in Department of Mechanical Engineering at the Pennsylvania State University. Dr. Gupta's research experience and interests include applications of the concepts of Statistical mechanics to understand the behavior and mechanisms of complex systems, Self-organization and stability analysis of multi-agent complex network systems, Adaptive coverage planning for terrain search using multiple robots, Applications of the methods of Symbolic dynamics for pattern recognition in complex systems, Fault detection, isolation and estimation in systems consisting of multiple interconnected subsystems such as an aircraft gas turbine engine, and in situ ultrasonic monitoring of micro structural flaws in mechanical systems. Dr. Gupta has authored or co-authored over thirty five research publications including seventeen scholarly articles in refereed journals, three book chapters and several international conference papers. Dr. Gupta is a member of American Society of Mechanical Engineers (ASME) and Institute of Electrical and Electronics Engineers (IEEE).

M. M. Mench obtained his PhD in Mechanical Engineering from Penn State University in 2000. After completing his post-doctoral research, he joined as a faculty member in the Department of Mechanical and Nuclear Engineering at Penn State in 2001, where he is presently an Associate Professor. His research interests include multiphase flow and transport in low temperature fuel cells, and other aspects of low temperature fuel cells related to stability and durability.

Asok Ray earned the Phd. degree in Mechanical Engineering from Northeastern University, Boston, MA, and also graduate degrees in each discipline of Electrical Engineering, Mathematics, and Computer Science. Dr. Ray joined the Pennsylvania State University in July 1985, and is currently a Distinguished Professor of Mechanical Engineering. Prior to joining Penn State, Dr. Ray held research and academic positions at Massachusetts Institute of Technology and Carnegie-Mellon University as well as research and management positions at GTE Strategic Systems Division, Charles Stark Draper Laboratory, and MITRE Corporation. Dr. Ray has been a Senior Research Fellow at NASA Glenn Research Center under a National Academy of Sciences award. Dr. Ray's research experience and interests include: Control and optimization of continuously varying and discrete-event dynamical systems; Intelligent instrumentation for real-time distributed systems; and Modeling and analysis of complex dynamical systems from thermodynamic perspectives in both deterministic and stochastic settings, as applied to Aeronautics and Astronautics, Undersea Vehicles and Surface Ships, Power and Processing plants, and Robotics. Dr. Ray has authored or co-authored over 400 research publications including about 220 scholarly articles in refereed journals such as transactions of ASME, IEEE and AIAA, and research monographs. Dr. Ray is a Fellow of IEEE, a Fellow of ASME, and a Fellow of World Innovative Foundation (WIF).